

# Flow and interferometry results from Au+Au collisions at $\sqrt{s_{\text{NN}}} = 4.5$ GeV

J. Adam<sup>6</sup>, L. Adamczyk<sup>2</sup>, J. R. Adams<sup>39</sup>, J. K. Adkins<sup>30</sup>, G. Agakishiev<sup>28</sup>, M. M. Aggarwal<sup>41</sup>, Z. Ahammed<sup>61</sup>, I. Alekseev<sup>3,35</sup>, D. M. Anderson<sup>55</sup>, A. Aparin<sup>28</sup>, E. C. Aschenauer<sup>6</sup>, M. U. Ashraf<sup>11</sup>, F. G. Atetalla<sup>29</sup>, A. Attri<sup>41</sup>, G. S. Averichev<sup>28</sup>, V. Bairathi<sup>53</sup>, K. Barish<sup>10</sup>, A. Behera<sup>52</sup>, R. Bellwied<sup>20</sup>, A. Bhasin<sup>27</sup>, J. Bielcik<sup>14</sup>, J. Bielcikova<sup>38</sup>, L. C. Bland<sup>6</sup>, I. G. Bordyuzhin<sup>3</sup>, J. D. Brandenburg<sup>49,6</sup>, A. V. Brandin<sup>35</sup>, J. Butterworth<sup>45</sup>, H. Caines<sup>64</sup>, M. Calderón de la Barca Sánchez<sup>8</sup>, J. M. Campbell<sup>39</sup>, D. Cebra<sup>8</sup>, I. Chakaberia<sup>29,6</sup>, P. Chaloupka<sup>14</sup>, B. K. Chan<sup>9</sup>, F.-H. Chang<sup>37</sup>, Z. Chang<sup>6</sup>, N. Chankova-Bunzarova<sup>28</sup>, A. Chatterjee<sup>11</sup>, D. Chen<sup>10</sup>, J. H. Chen<sup>18</sup>, X. Chen<sup>48</sup>, Z. Chen<sup>49</sup>, J. Cheng<sup>57</sup>, M. Cherney<sup>13</sup>, M. Chevalier<sup>10</sup>, S. Choudhury<sup>18</sup>, W. Christie<sup>6</sup>, X. Chu<sup>6</sup>, H. J. Crawford<sup>7</sup>, M. Csanád<sup>16</sup>, M. Daugherty<sup>1</sup>, T. G. Dedovich<sup>28</sup>, I. M. Deppner<sup>19</sup>, A. A. Derevschikov<sup>43</sup>, L. Didenko<sup>6</sup>, X. Dong<sup>31</sup>, J. L. Drachenberg<sup>1</sup>, J. C. Dunlop<sup>6</sup>, T. Edmonds<sup>44</sup>, N. Elsey<sup>63</sup>, J. Engelage<sup>7</sup>, G. Eppley<sup>45</sup>, R. Esha<sup>52</sup>, S. Esumi<sup>58</sup>, O. Evdokimov<sup>12</sup>, A. Ewigleben<sup>32</sup>, O. Eyser<sup>6</sup>, R. Fatemi<sup>30</sup>, S. Fazio<sup>6</sup>, P. Federic<sup>38</sup>, J. Fedorisin<sup>28</sup>, C. J. Feng<sup>37</sup>, Y. Feng<sup>44</sup>, P. Filip<sup>28</sup>, E. Finch<sup>51</sup>, Y. Fisyak<sup>6</sup>, A. Francisco<sup>64</sup>, L. Fulek<sup>2</sup>, C. A. Gagliardi<sup>55</sup>, T. Galatyuk<sup>15</sup>, F. Geurts<sup>45</sup>, A. Gibson<sup>60</sup>, K. Gopal<sup>23</sup>, D. Grosnick<sup>60</sup>, W. Guryn<sup>6</sup>, A. I. Hamad<sup>29</sup>, A. Hamed<sup>5</sup>, S. Harabasz<sup>15</sup>, J. W. Harris<sup>64</sup>, S. He<sup>11</sup>, W. He<sup>18</sup>, X. He<sup>26</sup>, S. Heppelmann<sup>8</sup>, S. Heppelmann<sup>42</sup>, N. Herrmann<sup>19</sup>, E. Hoffman<sup>20</sup>, L. Holub<sup>14</sup>, Y. Hong<sup>31</sup>, S. Horvat<sup>64</sup>, Y. Hu<sup>18</sup>, H. Z. Huang<sup>9</sup>, S. L. Huang<sup>52</sup>, T. Huang<sup>37</sup>, X. Huang<sup>57</sup>, T. J. Humanic<sup>39</sup>, P. Huo<sup>52</sup>, G. Igo<sup>9</sup>, D. Isenhower<sup>1</sup>, W. W. Jacobs<sup>25</sup>, C. Jena<sup>23</sup>, A. Jentsch<sup>6</sup>, Y. Ji<sup>48</sup>, J. Jia<sup>6,52</sup>, K. Jiang<sup>48</sup>, S. Jowzaee<sup>63</sup>, X. Ju<sup>48</sup>, E. G. Judd<sup>7</sup>, S. Kabana<sup>53</sup>, M. L. Kabir<sup>10</sup>, S. Kagamaster<sup>32</sup>, D. Kalinkin<sup>25</sup>, K. Kang<sup>57</sup>, D. Kapukchyan<sup>10</sup>, K. Kauder<sup>6</sup>, H. W. Ke<sup>6</sup>, D. Keane<sup>29</sup>, A. Kechechyan<sup>28</sup>, M. Kelsey<sup>31</sup>, Y. V. Khyzhniak<sup>35</sup>, D. P. Kikola<sup>62</sup>, C. Kim<sup>10</sup>, B. Kimelman<sup>8</sup>, D. Kincses<sup>16</sup>, T. A. Kinghorn<sup>8</sup>, I. Kisel<sup>17</sup>, A. Kiselev<sup>6</sup>, A. Kisel<sup>62</sup>, M. Kocan<sup>14</sup>, L. Kochenda<sup>35</sup>, L. K. Kosarzewski<sup>14</sup>, L. Kozyra<sup>62</sup>, L. Kramarik<sup>14</sup>, P. Kravtsov<sup>35</sup>, K. Krueger<sup>4</sup>, N. Kulathunga Mudiyanse<sup>20</sup>, L. Kumar<sup>41</sup>, R. Kunnawalkam Elayavalli<sup>63</sup>, J. H. Kwasizur<sup>25</sup>, R. Lacey<sup>52</sup>, S. Lan<sup>11</sup>, J. M. Landgraf<sup>6</sup>, J. Lauret<sup>6</sup>, A. Lebedev<sup>6</sup>, R. Lednicky<sup>28</sup>, J. H. Lee<sup>6</sup>, Y. H. Leung<sup>31</sup>, C. Li<sup>48</sup>, W. Li<sup>50</sup>, W. Li<sup>45</sup>, X. Li<sup>48</sup>, Y. Li<sup>57</sup>, Y. Liang<sup>29</sup>, R. Licenik<sup>38</sup>, T. Lin<sup>55</sup>, Y. Lin<sup>11</sup>, M. A. Lisa<sup>39</sup>, F. Liu<sup>11</sup>, H. Liu<sup>25</sup>, P. Liu<sup>52</sup>, P. Liu<sup>50</sup>, T. Liu<sup>64</sup>, X. Liu<sup>39</sup>, Y. Liu<sup>55</sup>, Z. Liu<sup>48</sup>, T. Ljubicic<sup>6</sup>, W. J. Llope<sup>63</sup>, R. S. Longacre<sup>6</sup>, N. S. Lukow<sup>54</sup>, S. Luo<sup>12</sup>, X. Luo<sup>11</sup>, G. L. Ma<sup>50</sup>, L. Ma<sup>18</sup>, R. Ma<sup>6</sup>, Y. G. Ma<sup>50</sup>, N. Magdy<sup>12</sup>, R. Majka<sup>64</sup>, D. Mallick<sup>36</sup>, S. Margetis<sup>29</sup>, C. Markert<sup>56</sup>, H. S. Matis<sup>31</sup>, J. A. Mazer<sup>46</sup>, K. Meehan<sup>8</sup>, N. G. Minaev<sup>43</sup>, S. Mioduszewski<sup>55</sup>, B. Mohanty<sup>36</sup>, M. M. Mondal<sup>52</sup>, I. Mooney<sup>63</sup>, Z. Moravcova<sup>14</sup>, D. A. Morozov<sup>43</sup>, M. Nagy<sup>16</sup>, J. D. Nam<sup>54</sup>, Md. Nasim<sup>22</sup>, K. Nayak<sup>11</sup>, D. Neff<sup>9</sup>, J. M. Nelson<sup>7</sup>, D. B. Nemes<sup>64</sup>, M. Nie<sup>49</sup>, G. Nigmatkulov<sup>35</sup>, T. Niida<sup>58</sup>, L. V. Nogach<sup>43</sup>, T. Nonaka<sup>58</sup>, A. S. Nunes<sup>6</sup>, G. Odyniec<sup>31</sup>, A. Ogawa<sup>6</sup>, S. Oh<sup>31</sup>, V. A. Okorokov<sup>35</sup>, B. S. Page<sup>6</sup>, R. Pak<sup>6</sup>, A. Pandav<sup>36</sup>, Y. Panebratsev<sup>28</sup>, B. Pawlik<sup>40</sup>, D. Pawlowska<sup>62</sup>, H. Pei<sup>11</sup>, C. Perkins<sup>7</sup>, L. Pinsky<sup>20</sup>, R. L. Pinter<sup>16</sup>, J. Pluta<sup>62</sup>, J. Porter<sup>31</sup>, M. Posik<sup>54</sup>, N. K. Pruthi<sup>41</sup>, M. Przybycien<sup>2</sup>, J. Putschke<sup>63</sup>, H. Qiu<sup>26</sup>, A. Quintero<sup>54</sup>, S. K. Radhakrishnan<sup>29</sup>, S. Ramachandran<sup>30</sup>, R. L. Ray<sup>56</sup>, R. Reed<sup>32</sup>, H. G. Ritter<sup>31</sup>, J. B. Roberts<sup>45</sup>, O. V. Rogachevskiy<sup>28</sup>, J. L. Romero<sup>8</sup>, L. Ruan<sup>6</sup>, J. Rusnak<sup>38</sup>, N. R. Sahoo<sup>49</sup>, H. Sako<sup>58</sup>, S. Salur<sup>46</sup>, J. Sandweiss<sup>64</sup>, S. Sato<sup>58</sup>, W. B. Schmidke<sup>6</sup>, N. Schmitz<sup>33</sup>, B. R. Schweid<sup>52</sup>, F. Seck<sup>15</sup>, J. Seger<sup>13</sup>, M. Sergeeva<sup>9</sup>, R. Seto<sup>10</sup>, P. Seyboth<sup>33</sup>, N. Shah<sup>24</sup>, E. Shahaliev<sup>28</sup>, P. V. Shanmuganathan<sup>6</sup>, M. Shao<sup>48</sup>, F. Shen<sup>49</sup>, W. Q. Shen<sup>50</sup>, S. S. Shi<sup>11</sup>, Q. Y. Shou<sup>50</sup>, E. P. Sichtermann<sup>31</sup>, R. Sikora<sup>2</sup>, M. Simko<sup>38</sup>, J. Singh<sup>41</sup>, S. Singha<sup>26</sup>, N. Smirnov<sup>64</sup>, W. Solyst<sup>25</sup>, P. Sorensen<sup>6</sup>, H. M. Spinka<sup>4</sup>, B. Srivastava<sup>44</sup>, T. D. S. Stanislaus<sup>60</sup>, M. Stefaniak<sup>62</sup>, D. J. Stewart<sup>64</sup>, M. Strikhanov<sup>35</sup>, B. Stringfellow<sup>44</sup>, A. A. P. Suaide<sup>47</sup>, M. Sumera<sup>38</sup>, B. Summa<sup>42</sup>, X. M. Sun<sup>11</sup>, X. Sun<sup>12</sup>, Y. Sun<sup>48</sup>, Y. Sun<sup>21</sup>, B. Surrow<sup>54</sup>, D. N. Svirida<sup>3</sup>, P. Szymanski<sup>62</sup>, A. H. Tang<sup>6</sup>, Z. Tang<sup>48</sup>, A. Taranenko<sup>35</sup>, T. Tarnowsky<sup>34</sup>, J. H. Thomas<sup>31</sup>, A. R. Timmins<sup>20</sup>, D. Tlusty<sup>13</sup>, M. Tokarev<sup>28</sup>, C. A. Tomkiel<sup>32</sup>, S. Trentalange<sup>9</sup>, R. E. Tribble<sup>55</sup>, P. Tribedy<sup>6</sup>, S. K. Tripathy<sup>16</sup>, O. D. Tsai<sup>9</sup>, Z. Tu<sup>6</sup>, T. Ullrich<sup>6</sup>, D. G. Underwood<sup>4</sup>, I. Upsal<sup>49,6</sup>, G. Van Buren<sup>6</sup>, J. Vanek<sup>38</sup>, A. N. Vasiliev<sup>43</sup>, I. Vassiliev<sup>17</sup>, F. Videbæk<sup>6</sup>, S. Vokal<sup>28</sup>, S. A. Voloshin<sup>63</sup>, F. Wang<sup>44</sup>, G. Wang<sup>9</sup>, J. S. Wang<sup>21</sup>, P. Wang<sup>48</sup>, Y. Wang<sup>11</sup>, Y. Wang<sup>57</sup>, Z. Wang<sup>49</sup>, J. C. Webb<sup>6</sup>, P. C. Weidenkaff<sup>19</sup>, L. Wen<sup>9</sup>, G. D. Westfall<sup>34</sup>, H. Wieman<sup>31</sup>, S. W. Wissink<sup>25</sup>, R. Witt<sup>59</sup>, Y. Wu<sup>10</sup>, Z. G. Xiao<sup>57</sup>, G. Xie<sup>31</sup>, W. Xie<sup>44</sup>, H. Xu<sup>21</sup>, N. Xu<sup>31</sup>, Q. H. Xu<sup>49</sup>, Y. F. Xu<sup>50</sup>, Y. Xu<sup>49</sup>, Z. Xu<sup>6</sup>, Z. Xu<sup>9</sup>, C. Yang<sup>49</sup>, Q. Yang<sup>49</sup>, S. Yang<sup>6</sup>, Y. Yang<sup>37</sup>, Z. Yang<sup>11</sup>, Z. Ye<sup>45</sup>, Z. Ye<sup>12</sup>, L. Yi<sup>49</sup>, K. Yip<sup>6</sup>, H. Zbroszczyk<sup>62</sup>, W. Zha<sup>48</sup>, D. Zhang<sup>11</sup>, S. Zhang<sup>48</sup>, S. Zhang<sup>50</sup>, X. P. Zhang<sup>57</sup>, Y. Zhang<sup>48</sup>, Y. Zhang<sup>11</sup>, Z. J. Zhang<sup>37</sup>, Z. Zhang<sup>6</sup>, Z. Zhang<sup>12</sup>, J. Zhao<sup>44</sup>, C. Zhong<sup>50</sup>, C. Zhou<sup>50</sup>, X. Zhu<sup>57</sup>, Z. Zhu<sup>49</sup>, M. Zurek<sup>31</sup>, M. Zyzak<sup>17</sup>

(STAR Collaboration)

<sup>1</sup>Abilene Christian University, Abilene, Texas 79699

<sup>2</sup>AGH University of Science and Technology, FPACS, Cracow 30-059, Poland

<sup>3</sup>Alikhanov Institute for Theoretical and Experimental Physics NRC "Kurchatov Institute", Moscow 117218, Russia

<sup>4</sup>Argonne National Laboratory, Argonne, Illinois 60439

- <sup>5</sup>*American University of Cairo, New Cairo 11835, New Cairo, Egypt*
- <sup>6</sup>*Brookhaven National Laboratory, Upton, New York 11973*
- <sup>7</sup>*University of California, Berkeley, California 94720*
- <sup>8</sup>*University of California, Davis, California 95616*
- <sup>9</sup>*University of California, Los Angeles, California 90095*
- <sup>10</sup>*University of California, Riverside, California 92521*
- <sup>11</sup>*Central China Normal University, Wuhan, Hubei 430079*
- <sup>12</sup>*University of Illinois at Chicago, Chicago, Illinois 60607*
- <sup>13</sup>*Creighton University, Omaha, Nebraska 68178*
- <sup>14</sup>*Czech Technical University in Prague, FNSPE, Prague 115 19, Czech Republic*
- <sup>15</sup>*Technische Universität Darmstadt, Darmstadt 64289, Germany*
- <sup>16</sup>*ELTE Eötvös Loránd University, Budapest, Hungary H-1117*
- <sup>17</sup>*Frankfurt Institute for Advanced Studies FIAS, Frankfurt 60438, Germany*
- <sup>18</sup>*Fudan University, Shanghai, 200433*
- <sup>19</sup>*University of Heidelberg, Heidelberg 69120, Germany*
- <sup>20</sup>*University of Houston, Houston, Texas 77204*
- <sup>21</sup>*Huzhou University, Huzhou, Zhejiang 313000*
- <sup>22</sup>*Indian Institute of Science Education and Research (IISER), Berhampur 760010, India*
- <sup>23</sup>*Indian Institute of Science Education and Research (IISER) Tirupati, Tirupati 517507, India*
- <sup>24</sup>*Indian Institute Technology, Patna, Bihar 801106, India*
- <sup>25</sup>*Indiana University, Bloomington, Indiana 47408*
- <sup>26</sup>*Institute of Modern Physics, Chinese Academy of Sciences, Lanzhou, Gansu 730000*
- <sup>27</sup>*University of Jammu, Jammu 180001, India*
- <sup>28</sup>*Joint Institute for Nuclear Research, Dubna 141 980, Russia*
- <sup>29</sup>*Kent State University, Kent, Ohio 44242*
- <sup>30</sup>*University of Kentucky, Lexington, Kentucky 40506-0055*
- <sup>31</sup>*Lawrence Berkeley National Laboratory, Berkeley, California 94720*
- <sup>32</sup>*Lehigh University, Bethlehem, Pennsylvania 18015*
- <sup>33</sup>*Max-Planck-Institut für Physik, Munich 80805, Germany*
- <sup>34</sup>*Michigan State University, East Lansing, Michigan 48824*
- <sup>35</sup>*National Research Nuclear University MEPhI, Moscow 115409, Russia*
- <sup>36</sup>*National Institute of Science Education and Research, HBNI, Jatni 752050, India*
- <sup>37</sup>*National Cheng Kung University, Tainan 70101*
- <sup>38</sup>*Nuclear Physics Institute of the CAS, Rez 250 68, Czech Republic*
- <sup>39</sup>*Ohio State University, Columbus, Ohio 43210*
- <sup>40</sup>*Institute of Nuclear Physics PAN, Cracow 31-342, Poland*
- <sup>41</sup>*Panjab University, Chandigarh 160014, India*
- <sup>42</sup>*Pennsylvania State University, University Park, Pennsylvania 16802*
- <sup>43</sup>*NRC "Kurchatov Institute", Institute of High Energy Physics, Protvino 142281, Russia*
- <sup>44</sup>*Purdue University, West Lafayette, Indiana 47907*
- <sup>45</sup>*Rice University, Houston, Texas 77251*
- <sup>46</sup>*Rutgers University, Piscataway, New Jersey 08854*
- <sup>47</sup>*Universidade de São Paulo, São Paulo, Brazil 05314-970*
- <sup>48</sup>*University of Science and Technology of China, Hefei, Anhui 230026*
- <sup>49</sup>*Shandong University, Qingdao, Shandong 266237*
- <sup>50</sup>*Shanghai Institute of Applied Physics, Chinese Academy of Sciences, Shanghai 201800*
- <sup>51</sup>*Southern Connecticut State University, New Haven, Connecticut 06515*
- <sup>52</sup>*State University of New York, Stony Brook, New York 11794*
- <sup>53</sup>*Instituto de Alta Investigación, Universidad de Tarapacá, Chile*
- <sup>54</sup>*Temple University, Philadelphia, Pennsylvania 19122*
- <sup>55</sup>*Texas A&M University, College Station, Texas 77843*
- <sup>56</sup>*University of Texas, Austin, Texas 78712*
- <sup>57</sup>*Tsinghua University, Beijing 100084*
- <sup>58</sup>*University of Tsukuba, Tsukuba, Ibaraki 305-8571, Japan*
- <sup>59</sup>*United States Naval Academy, Annapolis, Maryland 21402*
- <sup>60</sup>*Valparaiso University, Valparaiso, Indiana 46383*
- <sup>61</sup>*Variable Energy Cyclotron Centre, Kolkata 700064, India*
- <sup>62</sup>*Warsaw University of Technology, Warsaw 00-661, Poland*
- <sup>63</sup>*Wayne State University, Detroit, Michigan 48201 and*
- <sup>64</sup>*Yale University, New Haven, Connecticut 06520*

(Dated: May 15, 2022)

The Beam Energy Scan (BES) program at the Relativistic Heavy Ion Collider (RHIC) was extended to energies below  $\sqrt{s_{NN}} = 7.7$  GeV in 2015 by successful implementation of the fixed-target

mode of operation in the STAR (Solenoidal Track At RHIC) experiment. In the fixed-target mode, ions circulate in one ring of the collider and interact with a stationary target at the entrance of the STAR Time Projection Chamber. The first results for Au+Au collisions at  $\sqrt{s_{NN}} = 4.5$  GeV are presented, including directed and elliptic flow of identified hadrons, and radii from pion femtoscopy. The proton flow and pion femtoscopy results agree quantitatively with earlier measurements by Alternating Gradient Synchrotron experiments at similar energies. This validates running the STAR experiment in the fixed-target configuration. Pion directed and elliptic flow are presented for the first time at this beam energy. Pion and proton elliptic flow show behavior which hints at constituent quark scaling, but large error bars preclude reliable conclusions. The ongoing second phase of BES (BES-II) will provide fixed-target data sets with 100 times more events at each of several energies down to  $\sqrt{s_{NN}} = 3.0$  GeV.

PACS numbers: 25.75.-q, 25.75.Ag, 25.75.Dw, 25.75.Gz, 25.75.Ld, 25.75.Nq

## I. INTRODUCTION

The BES program at RHIC was undertaken to study the nature of the Quantum Chromodynamics (QCD) phase diagram in the plane of temperature versus baryon chemical potential, which is explored by varying the collision energy. The phase diagram region of current interest, at relatively high baryon chemical potential, is not accessible so far by first-principle lattice QCD calculations, and there is a wide-ranging international effort to investigate it experimentally [1]. The BES-II program, begun in 2019, covers collision energies at and below 19.6 GeV. The lowest energy which is accessible at RHIC with adequate luminosity is 7.7 GeV in the collider mode of operation. Therefore a fixed-target (FXT) program has been developed to allow the STAR experiment to access energies below 7.7 GeV. In this paper, results are presented from a first run using a single RHIC beam at injection energy incident on a gold target inside STAR beam-pipe, providing Au+Au collisions at  $\sqrt{s_{NN}} = 4.5$  GeV. Similar Au+Au collision energies were studied during the heavy-ion program at the Alternating Gradient Synchrotron (AGS) in the 1990s [2], with a top center of mass energy per nucleon pair ( $\sqrt{s_{NN}}$ ) of 4.9 GeV.

The present measurements of heavy-ion collisions at 4.5 GeV with STAR in fixed-target mode provide complementary views of the phase diagram to those from collider mode data, and extend the systematics of the world data on a number of observables at these energies. Characteristics of quark-gluon plasma (QGP), including the nature of the transition between QGP and hadronic matter [3–9], can be explored via measurements of azimuthal anisotropy with respect to the collision reaction plane (defined by the beam axis and the vector connecting the centers of the two colliding nuclei). This anisotropy is characterized by a series of Fourier coefficients [10–13]:

$$v_n = \langle \cos n(\phi - \Psi_R) \rangle, \quad (1)$$

where the angle brackets indicate an average over all events and particles of interest,  $\phi$  denotes the azimuthal angle of each particle,  $\Psi_R$  is the azimuthal angle of the reaction plane, and  $n$  denotes the harmonic number. The present study explores the first two harmonics: directed flow ( $v_1$ ) and elliptic flow ( $v_2$ ).

## II. PERFORMANCE IN FIXED TARGET MODE

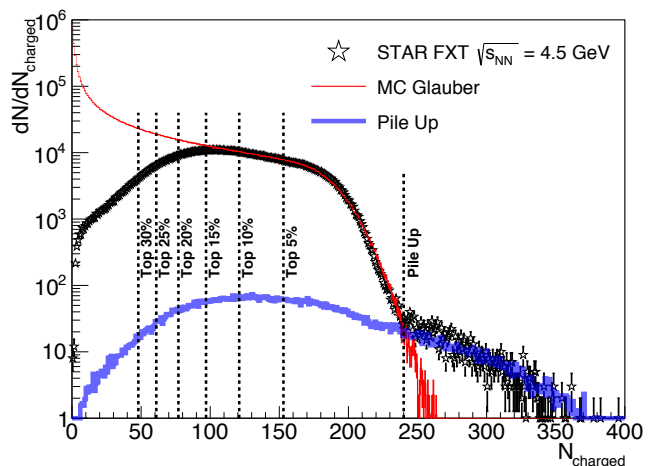


FIG. 1: (Color online) Centrality selection for STAR FXT  $\sqrt{s_{NN}} = 4.5$  GeV Au+Au collisions. The centrality variable  $N_{\text{charged}}$  is the number of tracks that pass the basic track cuts. The black points are the data, the thin red curve is the combined Monte-Carlo Glauber and negative binomial fit to the data, and the thick blue line is a Monte-Carlo model of pile-up events [14]. Vertical lines indicate the minimum number of tracks required for an event to be in the corresponding centrality bin. Events with multiplicity greater than 240 are dominated by pile-up, and are excluded from all analyses.

For the results reported in this paper, RHIC provided a single beam of gold ions with a kinetic energy of 8.9 GeV per nucleon in the laboratory frame. In this paper, the rapidity of a particle,  $y$ , is always given in the collision center-of-momentum frame, not the laboratory frame. The beam was incident on a gold target of thickness 1.93 g/cm<sup>2</sup> (1 mm), corresponding to a 1.7% interaction probability. The target was installed inside the vacuum pipe, below its center and 211 cm to the west of the center of the STAR detector. Central Au+Au events were recorded by requiring a coincidence between the downstream trigger detector, an arrangement of scintillator tiles called the Beam-Beam Counter (BBC) [15], and a high multiplicity signal in the time-of-flight (TOF) barrel [16]. About 1.3 million events with centrality 0-30%

TABLE I: The centrality selection used in the analyses. Included are the average number of participating nucleons ( $N_{\text{part}}$ ) estimated for the data for each centrality, the values of  $N_{\text{part}}$  predicted from a Glauber model for a minimum-bias trigger, the percentage of triggers corresponding to pile-up of two lower-multiplicity collisions, and the total number of events recorded. Each centrality corresponds to 5% of the total cross section.

Centrality (% of $\sigma_{\text{total}}$ )	$\langle N_{\text{part}} \rangle$ (Estimated)	$\langle N_{\text{part}} \rangle$ (Min bias)	Pile-up (%)	Events
0 - 5	$341 \pm 5$	336	1.35	266,694
5 - 10	$289 \pm 9$	286	0.72	267,347
10 - 15	$244 \pm 8$	242	0.58	258,854
15 - 20	$210 \pm 6$	204	0.49	203,600
20 - 25	$178 \pm 5$	170	0.44	125,539
25 - 30	$154 \pm 4$	142	0.40	68,844

were recorded.

The distribution of charged particle multiplicities is shown in Fig. 1. Also shown in the figure are the centrality selection criteria. The centrality class and the average number of participating nucleons, labeled  $\langle N_{\text{part}} \rangle$  (minimum bias) in Table I, were estimated using a Monte Carlo Glauber model [17] assuming a negative binomial distribution for charged particle production. Comparison of the Glauber Monte Carlo and the data indicates that the trigger efficiency approaches unity for the most central collisions, and therefore we take this as an assumption and estimate the trigger efficiencies for less central collisions from the ratio of the number of recorded events over 267,000 (the average number of events for the two most central bins). For the 0-5%, 5-10%, 10-15%, 15-20%, 20-25% and 25-30% bins, the efficiencies are 100%, 100%, 97%, 76%, 47% and 26%, respectively. The estimated  $\langle N_{\text{part}} \rangle$  for each bin is then determined by taking a weighted average of  $N_{\text{part}}$ , with weights equal to the number of recorded events for a given  $N_{\text{charged}}$ , calculated as a function of  $N_{\text{charged}}$  from the Glauber model.

Also shown in Fig. 1 is the estimated contribution of events which were the result of the pile-up of two minimum-bias collisions in the target from the same bunch. Due to the momentum resolution of the tracks and the projection distance back to the target (0.5 to 3.0 meters), the average distance of closest approach of a primary track to its vertex of origin is several millimeters. Thus, tracks from two separate collisions within the target would be reconstructed as emerging from a single vertex.

The location of the target along the beam axis was chosen to be  $z = 211$  cm (where  $z = 0$  corresponds to the center of the detector) in order to maximize the acceptance of the STAR Time Projection Chamber (TPC) [18] for fixed-target events. Protons and pions were selected from all charged tracks within a  $2\sigma$  band centered on the Bichsel prediction for  $dE/dx$  [19]. The acceptance is illustrated in Fig. 2 by the distribution of the measured  $p_T$  and rapidity for protons and pions.

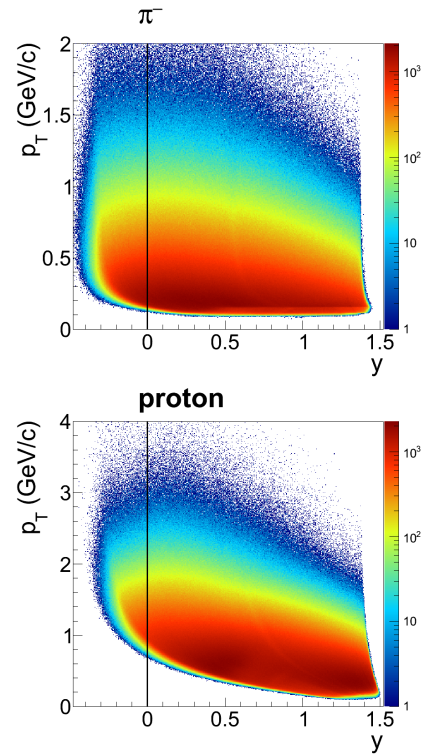


FIG. 2: Negative pion and proton relative yield versus rapidity and transverse momentum for STAR FXT  $\sqrt{s_{\text{NN}}} = 4.5$  GeV Au + Au collisions. The black line indicates the location of midrapidity. The target (beam) rapidity in the center of mass frame is at +1.52 (-1.52).

### III. DIRECTED FLOW

#### A. Proton and pion $v_1$

All directed flow analyses in this paper pertain only to rapidity-odd  $v_1(y)$ , which is a measure of the collective sideward deflection of emitted particles. The rapidity-even correlation  $v_1^{\text{even}}(y)$  [20, 21] is not related to the reaction plane in mass-symmetric collisions, and originates from initial-state event-by-event fluctuations.

We consider three distinct analysis methods: first, the TPC event plane (EP) approach with random sub-events for EP resolution correction [10–12]; second, a method based on the use of the Beam Beam Counter (BBC) detector for event plane determination [22–24]; and third, a direct calculation of multi-particle cumulants (the Q-cumulant method) [13]. Both the first and second methods use equation (1) to calculate the directed flow with the value of  $\Psi_R$  and its resolution estimated from a sub-event calculation based on information from either the TPC or the BBC [12]. The first method is less favored due in part to its susceptibility to bias from non-flow (correlations unrelated to the initial geometry of the collision) [13], but is investigated in the present proton directed flow study because that was the method used in 2000 by the E895 collaboration [25]. However, due to momentum

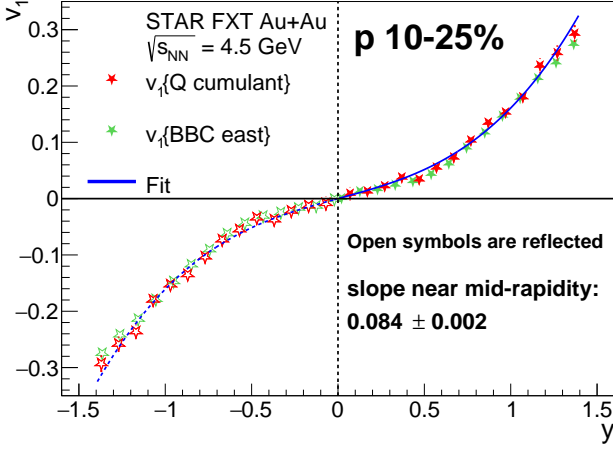


FIG. 3: Rapidity dependence of directed flow,  $v_1(y)$ , for protons with transverse momentum  $0.4 < p_T < 2.0$  GeV/ $c$  from events with 10-25% centrality. Two analysis methods, as discussed in the text, are compared. Plotted error bars are statistical only, and systematic errors are of comparable size. The curve is a cubic fit to the data.

conservation effects [26], this first method suffers from a relatively large departure from the  $v_1(y)$  odd function behavior required by symmetry, and only the second and third methods are presented in Fig. 3.

More specifically, the red star markers in Fig. 3 present proton  $v_1(y)$  based on a 4th-order direct Q-cumulant calculation [13], which suppresses the contribution from non-flow. The tracks included in the analysis have transverse momentum  $0.4 < p_T < 2.0$  GeV/ $c$ , which matches the selection used by E895 at  $\sqrt{s_{NN}} = 4.3$  GeV [25] and by STAR in collider mode at  $\sqrt{s_{NN}} = 7.7 - 200$  GeV [24]. Our centrality selection is 10-25%, which is consistent with the centrality reported by the E895 collaboration [25]. Due to the restricted acceptance and particle identification performance of the STAR detector in FXT mode (see Fig. 2), measurements are reported for only one side of midrapidity, and the odd-function behavior of directed flow is used to reflect points to the missing rapidity region.

The east-west asymmetry of FXT mode requires us to rely on the east BBC detector for the event plane estimation. Sub-event correlations between the east inner BBC (covering pseudorapidity 3.3 to 5) and the TPC [12] are used to correct for event plane resolution. The averaged east BBC event plane resolution for the slightly wider 10-30% centrality bin used in the pion directed flow analysis is  $41.4 \pm 0.4\%$ .

The shape of  $v_1(y)$  at  $\sqrt{s_{NN}} = 4.5$  GeV is described quite well by a cubic function  $Fy + F_3y^3$ , where  $F$  and  $F_3$  are constants extracted from a fit to the data. In order to study trends in proton directed flow as a function of beam energy, we take the linear term,  $F = dv_1/dy|_{y=0}$ , to characterize the overall strength of the directed flow signal at each energy. This is the same procedure as used at

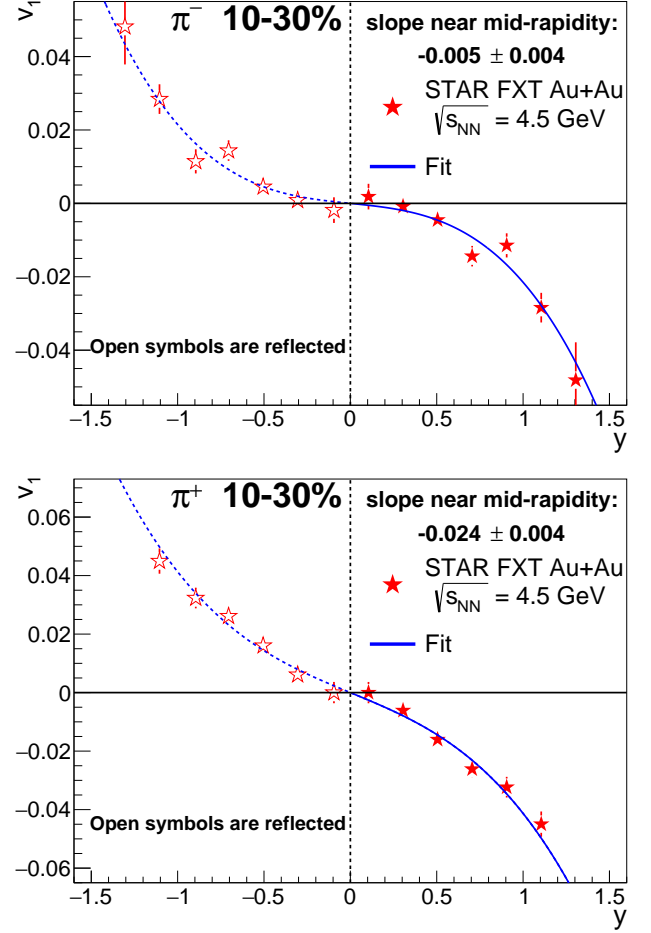


FIG. 4: Upper panel: Rapidity dependence of directed flow,  $v_1(y)$ , for negative pions with transverse momentum  $p_T > 0.2$  GeV/ $c$  and total momentum magnitude  $|p| < 1.6$  GeV/ $c$  from events within 10-30% centrality. Here, the BBC-based Event Plane method is used. Plotted error bars are statistical only, and systematic errors are of comparable size. The solid curve is a cubic fit to the data. Lower panel: The same for positive pions.

higher beam energies by STAR in collider mode [24] and at lower beam energies by E895 [25]. The curve in Fig. 3 shows the fit with  $F$  and  $F_3$  as free parameters. The extracted proton slope is  $dv_1/dy|_{y=0} = F = 0.084 \pm 0.002$ . In Ref. [27], the directed flow slope for ten particle species is presented for Au+Au collisions at  $\sqrt{s_{NN}} = 7.7$  to 200 GeV. As some of the species in Ref. [27] have relatively poor statistics, a more stable fit of the directed flow slopes in that analysis was obtained after requiring  $F_3 = 0$ . For the purpose of a consistent comparison with the slopes reported in Ref. [27], we also report the extracted proton slope with  $F_3 = 0$  in the present analysis, namely  $F = 0.086 \pm 0.002$  based on a fit over  $0 \leq y \leq 0.6$ .

Figure 4 presents  $v_1(y)$  for negative (upper panel) and positive (lower panel) pions using the BBC-based method referenced above. The 4th-order direct Q-cumulant method, as employed in Fig. 3, provides consistent re-



sults, but in the context of the relatively poor statistics for charged pions in FXT mode at  $\sqrt{s_{NN}} = 4.5$  GeV, the statistical errors on the BBC-based method are significantly smaller. No E895  $v_1$  measurements for pions were published, so the only available experimental data for comparison are STAR collider-mode measurements at  $\sqrt{s_{NN}} = 7.7$  GeV and above [24]. While track selections of transverse momentum  $p_T > 0.2$  GeV/ $c$  and total momentum magnitude  $|p| < 1.6$  GeV/ $c$  match the measurements at higher energies, the limited centrality range of our 2015 FXT test run restricts the centrality in Fig. 4 to 10-30%, and does not fully match the 10-40% centrality already published at  $\sqrt{s_{NN}} = 7.7$  GeV and above [24]. The blue line in Fig. 4 shows the fit with  $F$  and  $F_3$  as free parameters. The extracted negative pion slope is  $dv_1/dy|_{y=0} = F = -0.005 \pm 0.004$  and positive pion slope is  $dv_1/dy|_{y=0} = F = -0.024 \pm 0.004$ . For the purpose of a consistent comparison with slopes reported in Ref. [27], we also report the extracted negative and positive slopes with  $F_3 = 0$  in the present analysis, namely  $F = -0.013 \pm 0.003$  and  $F = -0.032 \pm 0.003$ , respectively, based on a fit over  $0 \leq y \leq 0.8$ .

The percentage difference between  $\pi^+$  and  $\pi^-$  directed flow becomes larger as we scan down from STAR collider energies to the present FXT energy point. This observation is consistent with isospin or Coulomb dynamics becoming more prominent at lower beam energies, and is qualitatively consistent with measurements at even lower energies reported by the FOPI collaboration [28].

Systematic errors arising from event-vertex cuts, particle ID cuts, and from contamination by other particle species, all make small to negligible contributions. Systematic errors arising from a cut on global distance of closest approach to the collision vertex, from the minimum number of hits required for  $dE/dx$  calculation, from the sensitivity to the fit range used when determining  $dv_1/dy$ , and from a correction for a region of diminishing proton acceptance near midrapidity, contribute at a level that is comparable to statistical errors.

### B. Lambda and Kaon $v_1$

Standard topological cuts on  $\pi^+\pi^-$  and  $p\pi^-$  pairs were utilized to identify  $K_S^0$  mesons and  $\Lambda$  baryons, respectively. Events with 10-30% centrality were selected for this analysis. The statistics of both  $K_S^0$  and  $\Lambda$  candidates are sufficient for the BBC or TPC event plane method with  $\eta$ -separated sub-events where the directed flow is calculated using Eq. (1). Two sub-event methods are used in this analysis. First, the event plane is reconstructed using BBC information (BBC event plane), and second, the event plane is reconstructed using primary protons and deuterons measured in the TPC with laboratory pseudorapidity  $-0.9 < \eta_{lab} < 0$  for every  $K_S^0$  or  $\Lambda$  candidate (TPC event plane). In the TPC event plane method, protons originating from  $\Lambda$  candidates are excluded from the event plane estimation in order to elimi-

nate self-correlation between  $\Lambda$  candidates and the event plane. Both TPC and BBC event plane resolutions are estimated using the method of three subevents [12]. The TPC event plane resolution is estimated to be  $67.5 \pm 0.5\%$  and the BBC event plane resolution to be  $40.0 \pm 0.5\%$ . The TPC event plane resolution can also be calculated [12] using the measured  $v_1$  and multiplicity of protons and deuterons that are used to reconstruct the event plane. With an assumption that  $v_1$  for deuterons is twice as large as for protons [29], the calculated resolution is 70.2%.

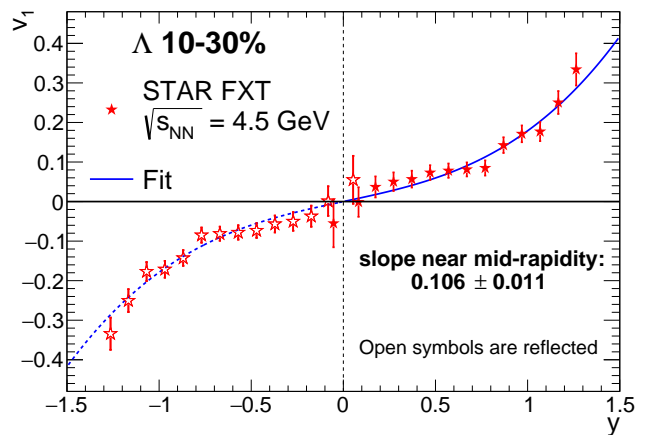


FIG. 5: The rapidity dependence of the directed flow for the  $\Lambda$  using the TPC event plane. Open symbols are the reflection of the solid symbols. The solid blue line is a cubic fit to the measured data. Plotted error bars are statistical only, while systematic errors are  $\pm 0.7 \times 10^{-2}$ .

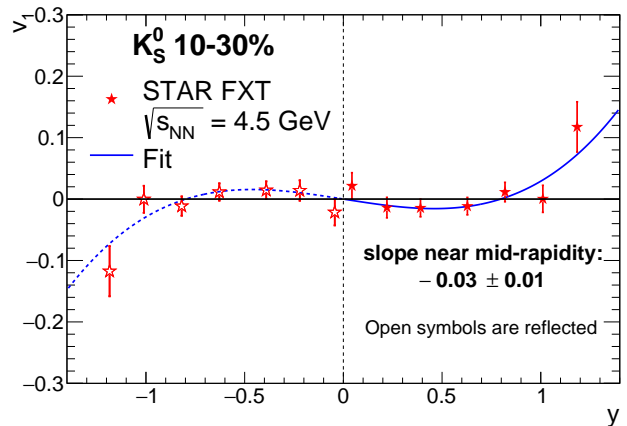


FIG. 6: The rapidity dependence of the directed flow for the  $K_S^0$  using the TPC event plane. Open symbols are the reflection of the solid symbols. The solid blue line is a cubic fit to the measured data. Plotted error bars are statistical only, while systematic errors are  $\pm 1.7 \times 10^{-2}$ .

The directed flow of  $\Lambda$  or  $K_S^0$  candidates is a superposition of a signal  $v_1(y)$  and a background  $v_1^B(y)$ . The

combination is  $v_1^{\text{tot}}(y) = v_1(y)\Delta S + v_1^B(y)\Delta B$ , where  $\Delta S$  is the fraction (relative to the total) of the  $\Lambda$  or  $K_S^0$  signal and  $\Delta B$  is the fraction of the combinatorial background accompanying the signal.  $\Delta S$  and its invariant mass resolution,  $\sigma_M$ , is calculated in every rapidity bin using the Pearson VII [30] function fit to the invariant mass spectrum of either  $\Lambda$  or  $K_S^0$  candidates after the combinatorial background, whose yield is reconstructed using the momentum rotation technique [31], is subtracted. Using equation (1), the flow of the combinatorial background,  $v_1^B(y)$ , is calculated from particle pairs outside the mass region of the  $K_S^0$  or  $\Lambda$ .

Figure 5 shows the directed flow of  $\Lambda$  hyperons. The horizontal positions of the data points are corrected for the width of the bin. Six different sets of topological cuts are employed, varying the total number of  $p\pi^-$  pairs from  $\sim 540K$  to  $\sim 160K$ , to observe how sensitive the directed flow of  $\Lambda$  is to the size of the statistical sample. Two invariant mass windows  $\pm 2\sigma_M$  and  $\pm 0.5\sigma_M$  are studied separately to vary the signal-to-background ratio, as well as the choice of either TPC or BBC event plane, to check if the event planes are consistent with each other.  $v_1^B(y)$  is calculated in both cases in the  $2 < |\sigma_M| < 5$  mass region outside of the center of the  $\Lambda$  peak. This gives a total of 24 results for slope parameters,  $F$ , representing the directed flow at midrapidity. Statistical errors on  $v_1$  come from the upper and lower limit of slopes calculated using the covariance matrices of the cubic fits to the directed flow data. The weighted average from these 24 fits is  $(10.6 \pm 1.1) \times 10^{-2}$  for  $\Lambda$  hyperons. The systematic uncertainty, calculated as the average of the differences between the mean value of  $10.6 \times 10^{-2}$  and the nominal values from the fits, is  $0.7 \times 10^{-2}$ .

The directed flow of  $K_S^0$  mesons was treated similarly, except wider binning was used and three invariant mass windows  $\pm 2\sigma_M$ ,  $\pm 1\sigma_M$ , and  $\pm 0.5\sigma_M$ .  $v_1^B(y)$  is calculated in all three cases in the  $2 < |\sigma_M| < 5$  mass region outside of the center of the  $K_S^0$  peak. In total,  $\sim 110K$   $\pi^+\pi^-$  pairs pass the tightest topological cuts, while  $\sim 370K$  pairs pass the loosest topological cuts. The weighted average of the total of 36 slope parameters  $F$  is  $(-3.4 \pm 1.1) \times 10^{-2}$  for  $K_S^0$  and the systematic uncertainty is  $1.7 \times 10^{-2}$ . The data points corrected for the bin widths are shown in Fig. 6.

### C. Beam Energy Dependence

Figure 7 presents slopes  $dv_1/dy|_{y=0}$ , based on the above-described cubic fits, for five species ( $p$ ,  $\Lambda$ ,  $K_S^0$ ,  $\pi^+$  and  $\pi^-$ ) measured in Au+Au collisions in FXT mode at  $\sqrt{s_{NN}} = 4.5$  GeV. Error bars show statistical uncertainties and shaded bands show systematic errors. The latter ones include factors already noted, as well as allowance for the rapidity range used in slope fitting.

Liu *et al.* [25] reported proton directed flow at central-ity 12-25% from the AGS E895 experiment, in the form of mean in-plane  $p_T$  and  $v_1(y)$  at  $\sqrt{s_{NN}} = 4.3$  GeV and be-

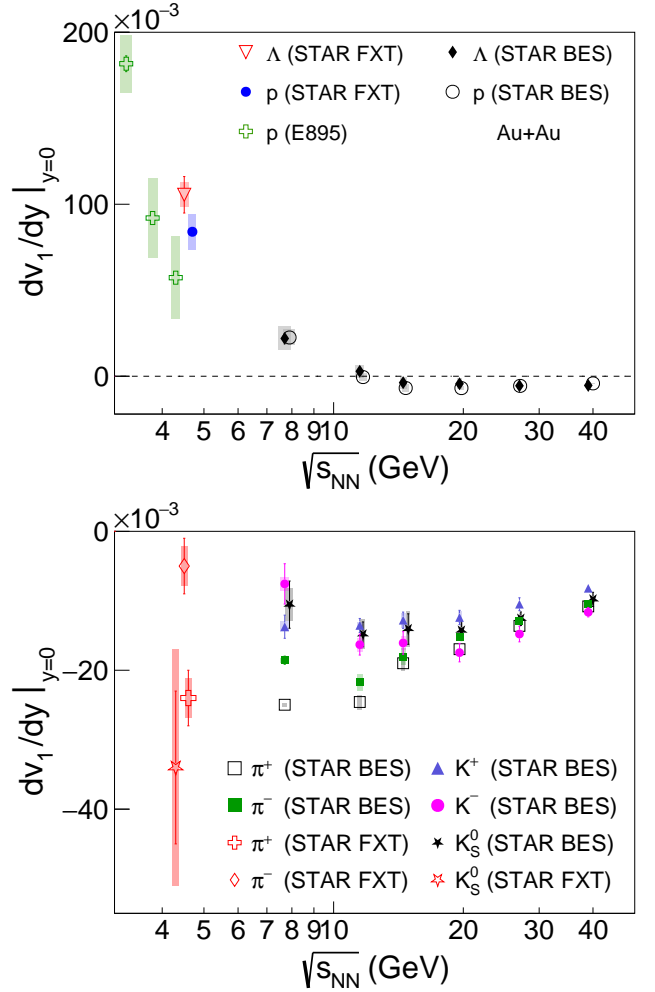


FIG. 7: (Color online) Beam energy dependence of the directed flow slope  $dv_1/dy$  at midrapidity for baryons (upper plot) and mesons (lower plot) measured by STAR (this paper and Refs. [24, 27]) and by AGS experiment E895 [25, 32]. Some points are slightly offset horizontally.

low. In order to compare  $dv_1/dy|_{y=0}$  between STAR and E895, it is necessary to carry out a cubic fit to E895  $v_1(y)$  for protons using similar criteria as for STAR  $v_1(y)$ . The E895 fitted slopes in the upper plot of Fig. 7 show statistical and systematic errors, where the latter arise from details of the fit. The E895 proton slopes reproduced in Ref. [24] are different, although consistent within errors, in part because Ref. [24] assumed errors on E895  $v_1(y)$  points that were equal to the marker size in cases where the actual errors were smaller than the published markers.

Note that the new proton  $v_1(y)$  slope measurement at  $\sqrt{s_{NN}} = 4.5$  GeV lies within errors on an interpolation between the same observable from STAR's published results for collider mode [24, 27] and E895 [25]. The highest E895 energy point at  $\sqrt{s_{NN}} = 4.3$  GeV agrees with the current FXT measurement within the uncertainties. Proton and  $\Lambda$  directed flow agree within errors at  $\sqrt{s_{NN}} =$

4.5 GeV. The  $\Lambda$  directed flow results fit into a pattern that was observed by STAR at  $\sqrt{s_{NN}} = 7.7$  GeV and above [27], but not at E895 energy points for  $\sqrt{s_{NN}} = 3.8, 3.3$  and 2.7 GeV [32].

Positively charged pions, negative pions, and neutral kaons all show directed flow ( $v_1$ ) signals in the opposite direction from that of the baryons, continuing trends observed at higher energies. The difference between  $\pi^+$  and  $\pi^-$  flow becomes stronger as the collision energy is reduced, which might be caused by isospin or Coulomb dynamics.

#### IV. ELLIPTIC FLOW OF PROTONS AND PIONS

The second term in the Fourier decomposition of the azimuthal distribution, an elliptic flow  $v_2$ , of identified particles (protons and pions) measured in Au+Au collisions at  $\sqrt{s_{NN}} = 4.5$  GeV, is discussed in this section. Elliptic flow of protons is compared with the earlier AGS data, while elliptic flow of pions had not been measured at this beam energy before. The appearance of number of constituent quark (NCQ) scaling, i.e. the collapse of quark-number-scaled flow strengths for mesons and baryons onto a single curve, is considered to be evidence of QGP formation [33, 34]. Further and more detailed exploration of the energy region where NCQ scaling is not present is very interesting, as it might provide characterisation of relevant observables at the lower energies, where creation of QGP is in question. Protons, which have been analyzed at a similar energy by the E895 experiment at the AGS [35], are compared to the previously published results from this experiment, while pions could only be compared to the results at higher energies. (Note that the results for protons at higher energies are published [36, 37]). Both positively and negatively charged pions are investigated separately in this analysis and it is found that they show the same behavior within uncertainties. Therefore, in the final plots positive and negative pions are presented together to improve the statistical significance of the result.

In this analysis of elliptic flow, two methods are used: (1) the event plane method using TPC information [10–12] and (2) the two-particle cumulants method [13]. The event plan resolution is about 20 %. Resonance decays generate unrelated correlations of particles in the final state. Such correlations are a non-flow contribution and they bias the elliptic flow measurement. Since particles from resonance decays are correlated both in  $\eta$  and  $\phi$ , we can reduce the non-flow contribution caused by resonances by measuring elliptic flow using particles which are not correlated in  $\eta$ . The implementation of this idea is different in each method. For the event plane method, we divide each event into two sub-events. For the cumulant method, we require a 0.1 gap in  $\eta$  between all considered pairs. Both methods give results which are consistent within their uncertainties.

Figure 8 shows the elliptic flow  $v_2$  as functions of transverse kinetic energy  $m_T - m$  for pions and protons obtained with the event plane method, where  $m$  is mass and  $m_T = \sqrt{m^2 + p_T^2}$  is transverse mass. It is compared to E895 results [35] obtained using the same method. We analyze the 0-30% most central events. For pions and protons, we require  $|y| < 0.5$ . In this analysis, we use tracks with  $0.2 < p_T < 2.0$  GeV/c, but due to STAR acceptance in FXT mode at  $\sqrt{s_{NN}} = 4.5$  GeV, we could analyze only protons with higher values of  $p_T$ , namely  $p_T > 0.4$  GeV/c (see Fig. 2). The proton results are consistent with E895 results [35].

To test the NCQ scaling, we divide  $v_2$  and  $m_T - m$  (Fig. 8) by the number of constituent quarks (2 for protons and 3 for pions). The results are presented in Fig. 9. The observed scaling with the number of constituent quarks at 4.5 GeV is similar to what is observed for Au+Au at higher collision energies [36, 37]. The system created for Au+Au at  $\sqrt{s_{NN}} = 4.5$  GeV has, perhaps surprisingly, larger collectivity than expected, and there is no significant difference in identified particle elliptic flow behavior when compared to higher energies.

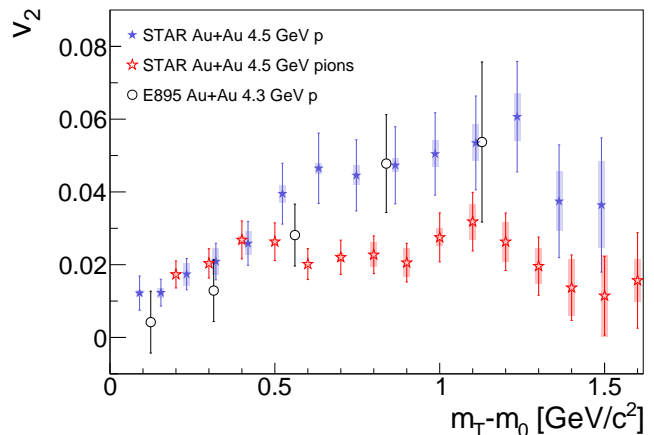


FIG. 8:  $v_2$  of protons and pions from STAR FXT data analysis, and  $v_2$  of protons from E895 experiment. Blue (red) stars represent STAR FXT proton (pion) data (0-30% centrality), and black circles show E895 data (12-25% centrality) [35].

Figure 10 shows the beam energy dependence of  $v_2$  measurements, integrated over  $p_T$ . The current results are consistent with the trends established by the previously published data.

#### V. FEMTOSCOPY OF PIONS

Two-particle correlations at low relative momentum can be used to extract information on the space-time structure of the particle-emitting source. Femtoscopy—the techniques of constructing and analyzing these correlations—has been performed in heavy-ion experiments over a broad range of energies [48].



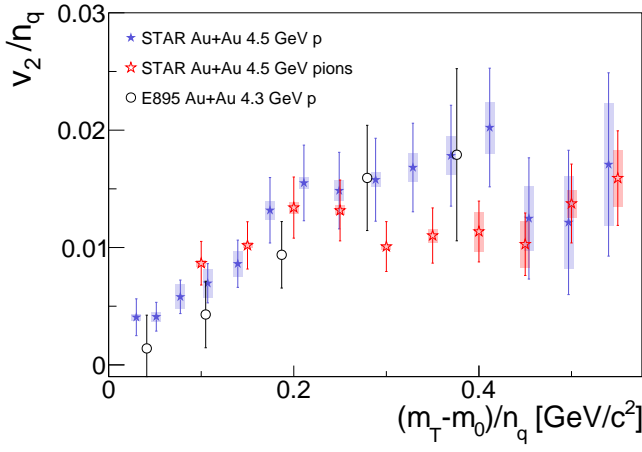


FIG. 9:  $v_2$  scaled by the number of constituent quarks ( $n_q$ ) for charged pions (red stars) and protons (blue stars) for 0-30% central collisions. The values of  $v_2$  scaled with  $n_q$  for pions and protons are consistent with each other within errors. For comparison, points from E895 are also shown (black circles)

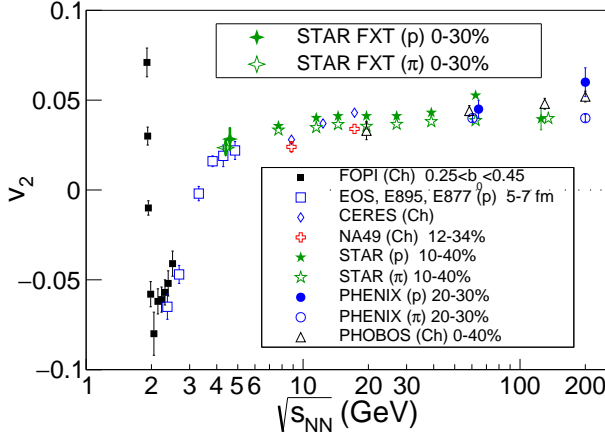


FIG. 10: The excitation function  $v_2$  for all charged particles or separately for protons and pions, measured by several experiments. The STAR FXT points for protons and for pions are near the region where a change in slope occurs. Data are shown from FOPI [38, 39], E895 [35], E877 [40], CERES [41], NA49 [42], PHENIX [43], PHOBOS [44], and from the STAR collider energies [36, 37, 45–47].

### A. Methodology

Femtoscopic correlation functions are formed by making distributions of the relative momenta  $\vec{q} \equiv \vec{p}_1 - \vec{p}_2$  of pairs of particles. A numerator distribution  $N(\vec{q})$  is formed using pairs where both tracks are from the same event, while a denominator distribution,  $D(\vec{q})$ , is formed by constructing pairs where the two tracks are from separate events, but having similar multiplicity and positions of the primary vertex; this is known as the “mixed-event” technique [49, 50]. The shape of both distributions will be dominated by the two-particle phase space distribution,

but  $N(\vec{q})$  will also contain contributions from Coulomb interactions and Bose-Einstein effects. The correlation function is the ratio

$$C(\vec{q}) = \frac{N(\vec{q})}{D(\vec{q})}. \quad (2)$$

This ratio is sensitive to the space-time structure of the pion emitting source [48, 51].

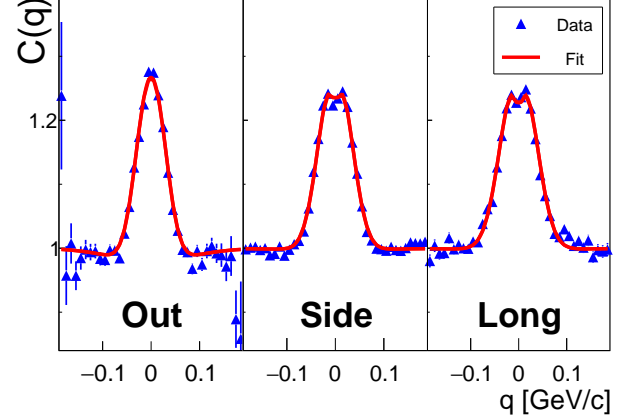


FIG. 11: Projections of the correlation functions in the LCMS frame onto the  $q_{out}$ ,  $q_{side}$ , and  $q_{long}$  axes for  $\pi^-\pi^-$  pairs from events in the 0-10% centrality range. Pairs are created from tracks in the momentum range  $0.1 < p_T < 0.3$  GeV/c. For each projection  $q_i$  shown, the other components of relative momentum are integrated over the range  $|q_j| < 35$  MeV/c. The red curve shows the projections [48] of a 3-dimensional fit to equation 4. Errors are statistical only.

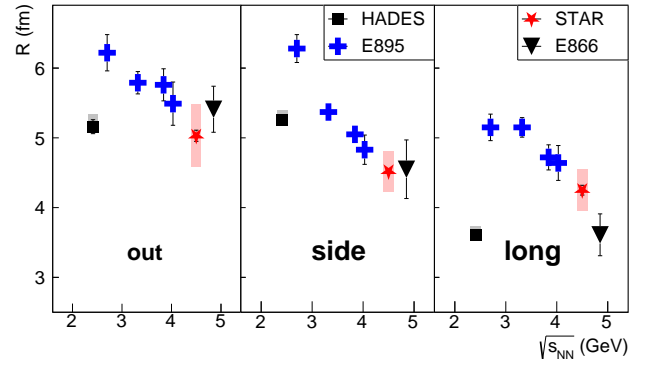


FIG. 12: Excitation function of  $R_{out}$ ,  $R_{side}$ , and  $R_{long}$  for four experiments: HADES [52], E895 [53], STAR, and E866 [54]. STAR points show both systematic (red boxes) and statistical errors (black lines) while errors for E895 and E866 are statistical only. HADES systematic errors are roughly the same size as the datapoints. The same momentum and centrality selections are applied as in Fig. 11.

Care must be taken to account for the effects of track reconstruction inefficiencies on the correlation function.

Single-track inefficiencies are common to both  $N(\vec{q})$  and  $D(\vec{q})$  and cancel in the ratio  $C(\vec{q})$ . However, two-track artifacts will affect  $N(\vec{q})$  alone, distorting  $C(\vec{q})$  at low  $|\vec{q}|$ . Track splitting (where hits from one charged particle are reconstructed as two distinct tracks) artificially enhances same-event pairs at low  $q$ . To eliminate this effect, we required both tracks to register separate hits on a minimum number of pad rows [47, 55, 56].

Track merging (where hits from two charged particles are reconstructed as one track) suppresses same-event low- $q$  pairs. These pairs cannot be recovered in the numerator  $N(\vec{q})$ , but similar pairs can be removed from the mixed-event distribution  $D(\vec{q})$  to compensate. To this end, we require all pairs to have a fraction of merged hits  $f_{\text{MH}} < 10\%$  [47, 55, 56]. All pair cuts are applied equally to  $N(\vec{q})$  and  $D(\vec{q})$ .

The relative momentum is evaluated in the Longitudinally Co-Moving System (LCMS), which is chosen such that  $(\vec{p}_1 + \vec{p}_2) \cdot \hat{z} = 0$ , where  $\hat{z}$  is the beam direction. The relative momentum  $\vec{q}$  is expressed in the Bertsch-Pratt [57–59] out-side-long coordinate system. The “longitudinal” direction,  $q_{\text{long}}$ , is taken to be the beam direction. The “out” direction,  $q_{\text{out}}$ , is taken to be the direction of the transverse component of the pair-momentum  $\vec{k}_T = (\vec{p}_1 + \vec{p}_2)/2$ , and the “side”,  $q_{\text{side}}$ , direction is defined to be perpendicular to the other two directions.

We use a Gaussian parameterization of the correlation function [60] to relate the experimental quantity in eq. (2) to the shape of the pion emitting source. The correlation function that would arise solely from quantum statistical effects is represented by the quantity  $C_{\text{free}}$  and can be expressed as

$$C_{\text{free}}(\vec{q}) = 1 + \exp(-R_{\text{out}}^2 q_{\text{out}}^2 - R_{\text{side}}^2 q_{\text{side}}^2 - R_{\text{long}}^2 q_{\text{long}}^2 - 2R_{\text{out-long}}^2 q_{\text{out}} q_{\text{long}}). \quad (3)$$

Here  $R_{\text{out}}$ ,  $R_{\text{side}}$ , and  $R_{\text{long}}$  give the lengths of the regions of homogeneity [61] in the out, side, and long directions, respectively. The cross term  $R_{\text{out-long}}^2$  represents a tilt of the correlation function in the  $q_{\text{out}} - q_{\text{long}}$  plane. To account for Coulomb interactions and contributions from halo pions we fit the data with the Bowler-Sinyukov functional form [47, 62, 63]:

$$C(\vec{q}) = (1 - \lambda) + \lambda K(q_{\text{inv}}) C_{\text{free}}(\vec{q}), \quad (4)$$

where  $\lambda$  is the fraction of pion pairs that carry a correlation signal (as opposed to, for instance, non-primary pions from resonance decays which are uncorrelated with pions from the fireball, at the resolution of our measurement). Electromagnetic final state interactions are quantified by  $K$ , the spatially-integrated squared Coulomb wave function. This function depends on the Lorentz invariant  $q_{\text{inv}} \equiv \sqrt{-q_\mu q^\mu}$ , where  $q_\mu = (E_1 - E_2, \vec{q})$ . The integral is taken over a spherical source 5 fm in radius [47, 64]. Integrating instead over a 3-fm source leads to negligible systematic error.

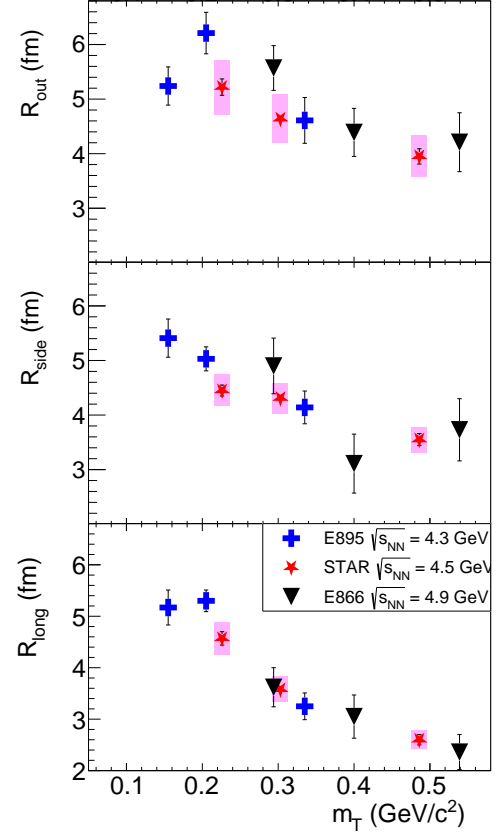


FIG. 13: Transverse mass dependence of  $R_{\text{out}}$ ,  $R_{\text{side}}$ , and  $R_{\text{long}}$  for three experiments: E895 [53], STAR, and E866 [54]. Pairs for the STAR points are created from negative pion tracks in the momentum range  $0.15 < p_T < 0.8$  GeV/c from events in the 0-15% centrality range. STAR points show both systematic (magenta boxes) and statistical errors (black lines) while errors for E895 and E866 are statistical only.

## B. Results

Figure 11 shows fits of the form in Eq. 4 (red lines) to the experimental correlation function defined in Eq. 2 (blue stars). The three panels show projections of the correlation function onto the  $q_{\text{out}}$ ,  $q_{\text{side}}$ , and  $q_{\text{long}}$  axes. Data here are for  $\pi^-\pi^-$  pairs created from tracks with transverse momentum  $0.1 < p_T < 0.3$  GeV/c, from events in the 0-10% centrality range. The transverse momentum of the pairs is required to be in the range  $0.15 < k_T < 0.6$  GeV/c. These cuts are chosen to match as closely as possible those in the E895 experiment, which used the same  $p_T$  cuts and corresponded to approximately 0-11% centrality [53]. There is a slight suppression at  $q_{\text{side}} \approx 0$  and  $q_{\text{long}} \approx 0$  due to the Coulomb repulsion of like-sign pion pairs. The three-dimensional fit reproduces the data reasonably well. The correlation functions are fit via maximum likelihood [48], but chi-square is often used as a measure of the fit. For the fit in

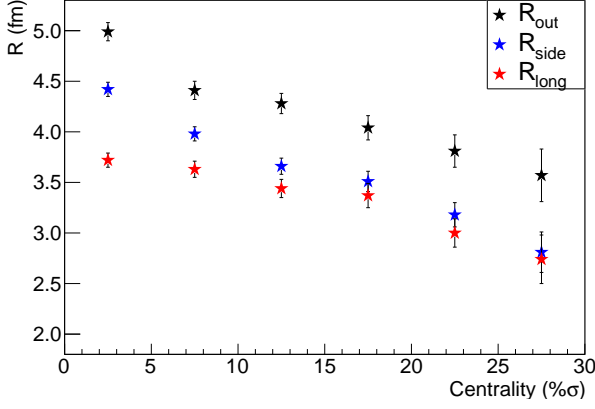


FIG. 14: The centrality dependence of  $R_{\text{out}}$ ,  $R_{\text{side}}$ , and  $R_{\text{long}}$ . Errors are statistical only. Here  $\pi^+\pi^+$  and  $\pi^-\pi^-$  pairs in the momentum range  $0.15 < p_T < 0.8$  GeV/ $c$  are used.

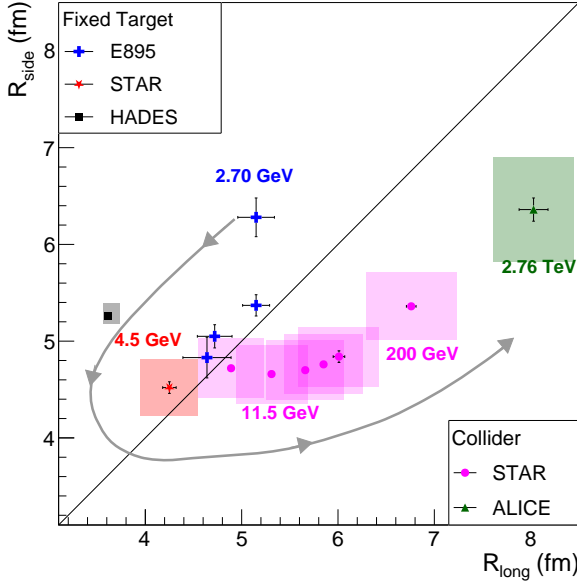


FIG. 15:  $R_{\text{side}}$  vs.  $R_{\text{long}}$ , which measures the prolate-ness/oblateness of the pion emitting source when viewed from beside the beam. HADES [52], ALICE [65] and STAR [66] points include systematic errors; E895 [53] show statistical errors only. The various centrality,  $p_T$ , and  $k_T$  cuts used in the different experiments are discussed in the text. For the STAR fixed-target point, the same momentum and centrality selection are applied as in figure 13. The grey curve indicates the evolution of the shape, as the collision energy is increased.

Fig. 11,  $\chi^2/\text{ndf} = 122272/108811 = 1.12$ . Fits discussed here have  $\chi^2/\text{ndf} = 1 - 2$ . While not perfect, these reasonable fits can be used to extract radii that characterize the spacetime extent of the source.

Figure 12 shows the excitation function of the three femtoscopic radii for the HADES [52], E895 [53], STAR,

and E866 [54] experiments. The comparison with data from E866 is complicated by several issues. Firstly, a different centrality definition was employed, and it is unclear how to translate this into the more commonly-used characterization of the fraction of the inelastic cross section. Secondly, the narrow spectrometer acceptance of E866 did not cover midrapidity (it covered  $-0.30 \lesssim y \lesssim -0.05$ ) and has a higher transverse momentum lower limit. Thirdly, unlike the other results to which we compare (and most other measurements), the  $m_T$ -dependent analysis was not performed in the LCMS. Nevertheless, the E866 results with the closest event and track selection criteria to the present results are included for context. The E895 and E866 points show a monotonically decreasing beam energy dependence. The fixed-target STAR points are consistent with this trend within the uncertainties.

The  $R_{\text{side}}$  radius primarily reflects the spatial extent of the pion emitting source, whereas  $R_{\text{out}}$  convolves this with the emission duration of the fireball [67–69]. Figure 13 shows the radii as functions of the transverse mass  $m_T = \sqrt{m_\pi^2 + k_T^2}$ , where  $m_\pi$  is the pion mass. In order to match analysis cuts from the E866 data, here the STAR points use a wider transverse momentum cut of  $0.15 < p_T < 0.8$  GeV/ $c$ , and include events from the 0–15% centrality range. The decrease in  $R_{\text{side}}$  and  $R_{\text{out}}$  with increasing  $m_T$  has been attributed to transverse flow, and the decrease in  $R_{\text{long}}$  is attributed to longitudinal flow [61, 68]. High- $m_T$  pairs come from smaller regions within the source and do not reflect the system’s overall size [66]. The STAR points agree very well with those from E895 and E866 for  $R_{\text{side}}$  and  $R_{\text{long}}$ , as well as for  $R_{\text{out}}$  at high  $m_T$ . For  $R_{\text{out}}$  the STAR points are slightly below E895 and E866 at low  $m_T$ , but agree within uncertainties.

Figure 14 shows the centrality dependence of the radii. Here we combine  $\pi^+\pi^+$  and  $\pi^-\pi^-$  pairs and use the wider transverse momentum range of  $0.15 < p_T < 0.8$  GeV/ $c$ . The radii decrease for more peripheral events due to the smaller geometric size of the initial participant region and the subsequent emission region at freezeout.

Figure 15 shows  $R_{\text{side}}$  vs.  $R_{\text{long}}$  for several different data sets: E895 Au+Au [53], STAR FXT Au+Au, STAR BES-I Au+Au [66], and ALICE Pb+Pb [65]. STAR FXT and BES points use low- $k_T$ ,  $\pi^+\pi^+$  and  $\pi^-\pi^-$  pion pairs, with  $\langle k_T \rangle \approx 0.22$  GeV/ $c$ . Events are drawn from the 0–5% centrality range. The ALICE point also corresponds to 0–5% centrality, but a slightly higher  $\langle k_T \rangle$  of  $\approx 0.26$  GeV/ $c$ . The E895 points use the cuts discussed above. The collision energies ( $\sqrt{s_{NN}}$ ) corresponding to each experiment are indicated in GeV. The significantly different acceptance and use of a different frame by E866 [54] affects the longitudinal radius in a way very different from that for the sideward. Hence, it makes little sense to include E866 data in a graph which plots  $R_{\text{side}}$  versus  $R_{\text{long}}$ ; it is not shown in Fig. 15, which is a direct comparison of similar measurements over three orders of magnitude in energy.

The figure indicates the prolateness/oblateness of the pion emitting source, as viewed from beside the beam. A high  $R_{\text{side}}$  and low  $R_{\text{long}}$  indicates a very prolate source, whereas the reverse indicates an oblate source. Lower energy collisions generally produce more prolate systems, and the shape of the emission region tends to become more oblate as the collision energy is increased. In this representation, the evolution follows a “swoosh” systematic, indicated by the grey curve drawn to guide the eye. This trend reflects the evolution from stopping-dominated dynamics at low collision energies, to the approximately longitudinally-boost-invariant scenario at the highest energies. The STAR fixed-target point has  $R_{\text{side}} \approx R_{\text{long}} \approx 4.5$  fm, indicating a source that is approximately round when viewed from the side, just at the transition point between oblate and prolate geometry.

## VI. SUMMARY

In this first set of results from fixed-target running at the STAR experiment, we report that the directed flow ( $v_1$ ) of protons and  $\Lambda$  baryons is in line with existing systematics at higher and lower energy. This is critically important, as the directed flow of net baryons [24, 27] is one of the most intriguing experimental results from the BES program, as well as one of the most difficult for models to explain.

We have also presented the first measurements of azimuthal anisotropy of charged pions and neutral kaons at these energies. Both show directed flow ( $v_1$ ) signals in the direction opposite to that of the baryons, continuing trends observed at higher energies. The difference between  $\pi^+$  and  $\pi^-$  flow becomes stronger as the collision energy is reduced, perhaps signaling important isospin or Coulomb dynamics. Interestingly, within the relatively large statistical uncertainties, the data are consistent with constituent quark scaling of elliptic flow, an effect proposed at much higher energies to arise from quark coalescence in the QGP phase.

Pion source radii based on femtoscopy agree quantitatively with previous measurements at the AGS, and with the broader systematic trends established at higher beam energies. They signal a transition region between oblate and prolate spatial sources.

Overall, while these measurements are important and of interest on their own, they also pave the way for the FXT energy scan with nominally one hundred times more events at each energy. The FXT energy scan is an integral part of the BES-II program at RHIC which began in early 2019. It extends the reach of the STAR experiment across an important energy regime of high baryon chemical potential, ranging from 420 to 720 MeV [70], corresponding to collision energies from 7.7 down to 3.0 GeV.

## VII. ACKNOWLEDGEMENTS

We acknowledge valuable discussions with Yasushi Nara and Horst Stöcker. We thank the RHIC Operations Group and RCF at BNL, the NERSC Center at LBNL, and the Open Science Grid consortium for providing resources and support. This work was supported in part by the Office of Nuclear Physics within the U.S. DOE Office of Science, the U.S. National Science Foundation, the Ministry of Education and Science of the Russian Federation, National Natural Science Foundation of China, Chinese Academy of Science, the Ministry of Science and Technology of China and the Chinese Ministry of Education, the Higher Education Sprout Project by Ministry of Education at NCKU, the National Research Foundation of Korea, Czech Science Foundation and Ministry of Education, Youth and Sports of the Czech Republic, Hungarian National Research, Development and Innovation Office, New National Excellency Programme of the Hungarian Ministry of Human Capacities, Department of Atomic Energy and Department of Science and Technology of the Government of India, the National Science Centre of Poland, the Ministry of Science, Education and Sports of the Republic of Croatia, RosAtom of Russia and German Bundesministerium für Bildung, Wissenschaft, Forschung und Technologie (BMBF), Helmholtz Association, Ministry of Education, Culture, Sports, Science, and Technology (MEXT) and Japan Society for the Promotion of Science (JSPS).

- 
- [1] T. Galatyuk, Nucl. Phys. **A982**, 163 (2019).
- [2] G. Rai et al. (E895 Collaboration), Nucl. Phys. A **661**, 162 (1999).
- [3] J. Steinheimer, J. Auvinen, H. Petersen, M. Bleicher, and H. Stöcker, Phys. Rev. C **89**, 054913 (2014).
- [4] V. P. Konchakovski, W. Cassing, Y. B. Ivanov, and V. D. Toneev, Phys. Rev. C **90**, 014903 (2014).
- [5] Y. B. Ivanov and A. A. Soldatov, Phys. Rev. C **91**, 024915 (2015).
- [6] Y. Nara, H. Niemi, J. Steinheimer, and H. Stöcker, Phys. Lett. B **769**, 543 (2017).
- [7] S. Singha, P. Shanmuganathan, and D. Keane, Adv. High Energy Phys. **2016**, 2836989 (2016).
- [8] Y. Nara, H. Niemi, A. Ohnishi, J. Steinheimer, X. Luo, and H. Stöcker, Eur. Phys. J. A **54**, 18 (2018).
- [9] Y. Nara, T. Maruyama, and H. Stöcker (2020), 2004.05550.
- [10] J.-Y. Ollitrault, Phys. Rev. D **46**, 229 (1992).
- [11] S. Voloshin and Y. Zhang, Z. Phys. C **70**, 665 (1996).
- [12] A. M. Poskanzer and S. A. Voloshin, Phys. Rev. C **58**, 1671 (1998).
- [13] A. Bilandzic, R. Snellings, and S. Voloshin, Phys. Rev. C **83**, 044913 (2011).
- [14] K. Meehan, Ph.D. thesis, University of California, Davis (2018), URL <https://drupal.star.bnl.gov/STAR/files/FinalThesis.pdf>.
- [15] E. G. Judd et al., Nucl. Instrum. and Meth. A **902**, 228 (2018).
- [16] W. Llope, Nucl. Instrum. and Meth. A **661**, S110 (2012).
- [17] R. Ray and M. Daugherty, J. Phys. G **35**, 125106 (2008).
- [18] M. Anderson et al., Nucl. Instrum. and Meth. A **499**, 659 (2003).
- [19] H. Bichsel, Nucl. Instrum. and Meth. A **562**, 154 (2006).
- [20] D. Teaney and L. Yan, Phys. Rev. C **83**, 064904 (2011).
- [21] M. Luzum and J.-Y. Ollitrault, Phys. Rev. Lett. **106**, 102301 (2011).
- [22] C. A. Whitten, AIP Conference Proceedings **980**, 390 (2008).
- [23] G. Agakishiev et al. (STAR Collaboration), Phys. Rev. C **85**, 014901 (2012).
- [24] L. Adamczyk et al. (STAR Collaboration), Phys. Rev. Lett. **112**, 162301 (2014).
- [25] H. Liu et al. (E895 Collaboration), Phys. Rev. Lett. **84**, 5488 (2000).
- [26] N. Borghini, P. M. Dinh, J.-Y. Ollitrault, A. M. Poskanzer, and S. A. Voloshin, Phys. Rev. C **66**, 014901 (2002).
- [27] L. Adamczyk et al. (STAR Collaboration), Phys. Rev. Lett. **120**, 062301 (2018).
- [28] W. Reisdorf et al. (FOPI Collaboration), Nucl. Phys. A **781**, 459 (2007).
- [29] S. Wang et al. (EOS Collaboration), Phys. Rev. Lett. **74**, 2646 (1995).
- [30] K. Pearson, Philosophical Transactions of the Royal Society of London. Series A, Containing Papers of a Mathematical or Physical Character **216**, 429 (1916).
- [31] B. I. Abelev et al. (STAR Collaboration), Science **328**, 58 (2010).
- [32] P. Chung et al. (E895 Collaboration), Phys. Rev. Lett. **86**, 2533 (2001).
- [33] J. Adams et al. (STAR Collaboration), Phys. Rev. Lett. **92**, 052302 (2004).
- [34] J. Tian, J. Chen, Y. Ma, X. Cai, F. Jin, G. Ma, S. Zhang, and C. Zhong, Phys. Rev. C **79**, 067901 (2009).
- [35] C. Pinkenburg et al. (E895 Collaboration), Phys. Rev. Lett. **83**, 1295 (1999).
- [36] L. Adamczyk et al. (STAR Collaboration), Phys. Rev. C **88**, 014902 (2013).
- [37] L. Adamczyk et al. (STAR Collaboration), Phys. Rev. C **93**, 014907 (2016).
- [38] W. Reisdorf et al. (FOPI Collaboration), Nucl. Phys. A **876**, 1 (2012).
- [39] A. Andronic et al. (FOPI Collaboration), Phys. Lett. B **612**, 173 (2005).
- [40] P. Braun-Munzinger and J. Stachel, Nucl. Phys. A **638**, 3c (1998).
- [41] H. Appelshäuser (CERES Collaboration), Nucl. Phys. A **698**, 253 (2002).
- [42] C. Alt et al. (NA49 Collaboration), Phys. Rev. C **68**, 034903 (2003).
- [43] A. Adare et al. (PHENIX Collaboration), Phys. Rev. C **92**, 034913 (2015).
- [44] B. B. Back et al. (PHOBOS Collaboration), Phys. Rev. Lett. **94**, 122303 (2005).
- [45] C. Adler et al. (STAR Collaboration), Phys. Rev. Lett. **87**, 182301 (2001).
- [46] J. Adams et al. (STAR Collaboration), Phys. Rev. C **72**, 014904 (2005).
- [47] J. Adams et al. (STAR Collaboration), Phys. Rev. C **71**, 044906 (2005).
- [48] M. A. Lisa, S. Pratt, R. Soltz, and U. Wiedemann, Annual Review of Nuclear and Particle Science **55**, 357 (2005).
- [49] G. I. Kopylov and M. I. Podgoretsky, Sov. J. Nucl. Phys. **15**, 219 (1972).
- [50] U. Heinz and B. V. Jacak, Annual Review of Nuclear and Particle Science **49**, 529 (1999).
- [51] G. Goldhaber, S. Goldhaber, W. Lee, and A. Pais, Phys. Rev. **120**, 300 (1960).
- [52] J. Adamczewski-Musch et al. (HADES), Phys. Lett. B **795**, 446 (2019).
- [53] M. A. Lisa et al. (E895 Collaboration), Phys. Rev. Lett. **84**, 2798 (2000).
- [54] L. Ahle et al. (E802 Collaboration), Phys. Rev. C **66**, 054906 (2002).
- [55] C. Adler et al. (STAR Collaboration), Phys. Rev. Lett. **87**, 082301 (2001).
- [56] J. Adams et al. (STAR Collaboration), Phys. Rev. Lett. **93**, 012301 (2004).
- [57] S. Pratt, Phys. Rev. D **33**, 1314 (1986).
- [58] G. Bertsch, M. Gong, and M. Tohyama, Phys. Rev. C **37**, 1896 (1988).
- [59] S. Chapman, P. Scotto, and U. Heinz, Phys. Rev. Lett. **74**, 4400 (1995).
- [60] U. Heinz, A. Hummel, M. A. Lisa, and U. A. Wiedemann, Phys. Rev. C **66**, 044903 (2002).
- [61] A. Makhlin and Y. Sinyukov, Z. Phys. C **39**, 69 (1988).
- [62] M. Bowler, Phys. Lett. B **270**, 69 (1991).
- [63] Y. Sinyukov, R. Lednicky, S. Akkelin, J. Pluta, and B. Erasmus, Phys. Lett. B **432**, 248 (1998).
- [64] B. I. Abelev et al. (STAR Collaboration), Phys. Rev. C **80**, 024905 (2009).



- [65] A. Aamodt et al. (ALICE Collaboration), Phys. Lett. B **696**, 328 (2011).
- [66] L. Adamczyk et al. (STAR Collaboration), Phys. Rev. C **92**, 014904 (2015).
- [67] E. Mount, G. Graef, M. Mitrovski, M. Bleicher, and M. A. Lisa, Phys. Rev. C **84**, 014908 (2011).
- [68] F. Retière and M. A. Lisa, Phys. Rev. C **70**, 044907 (2004).
- [69] D. Rischke and M. Gyulassy, Nucl. Phys. A **608**, 479 (1996).
- [70] J. Cleymans, H. Oeschler, K. Redlich, and S. Wheaton, Phys. Rev. C **73**, 034905 (2006).